



HAL
open science

Linking dissipation, anisotropy, and intermittency in rotating stratified turbulence at the threshold of linear shear instabilities

Annick Pouquet, Duane Rosenberg, R. Marino

► **To cite this version:**

Annick Pouquet, Duane Rosenberg, R. Marino. Linking dissipation, anisotropy, and intermittency in rotating stratified turbulence at the threshold of linear shear instabilities. *Physics of Fluids*, 2019, 31 (10), pp.105116. 10.1063/1.5114633 . hal-02392081

HAL Id: hal-02392081

<https://hal.science/hal-02392081v1>

Submitted on 20 Jan 2025

HAL is a multi-disciplinary open access archive for the deposit and dissemination of scientific research documents, whether they are published or not. The documents may come from teaching and research institutions in France or abroad, or from public or private research centers.

L'archive ouverte pluridisciplinaire **HAL**, est destinée au dépôt et à la diffusion de documents scientifiques de niveau recherche, publiés ou non, émanant des établissements d'enseignement et de recherche français ou étrangers, des laboratoires publics ou privés.



Distributed under a Creative Commons Attribution 4.0 International License

Linking dissipation, anisotropy, and intermittency in rotating stratified turbulence at the threshold of linear shear instabilities

A. Pouquet,^{1,2} D. Rosenberg,³  and R. Marino⁴ 

AFFILIATIONS

¹Laboratory for Atmospheric and Space Physics, University of Colorado, Boulder, Colorado 80309, USA

²National Center for Atmospheric Research, P.O. Box 3000, Boulder, Colorado 80307, USA

³1401 Bradley Dr., Boulder, Colorado 80305, USA

⁴Laboratoire de Mécanique des Fluides et d'Acoustique, CNRS, École Centrale de Lyon, Université Claude Bernard Lyon 1, INSA de Lyon, Écully F-69134, France

ABSTRACT

Analyzing a large database of high-resolution three-dimensional direct numerical simulations of decaying rotating stratified flows, we show that anomalous mixing and dissipation, marked anisotropy, and strong intermittency are all observed simultaneously in an intermediate regime of parameters in which both waves and eddies interact nonlinearly. A critical behavior governed by the stratification occurs at Richardson numbers of order unity and with the flow close to being in a state of instability. This confirms the central dynamical role, in rotating stratified turbulence, of large-scale intermittency, which occurs in the vertical velocity and temperature fluctuations, as an adjustment mechanism of the energy transfer in the presence of strong waves.

I. INTRODUCTION, EQUATIONS, AND DIAGNOSTICS

A signature of fully developed turbulence (FDT) is its intermittency, i.e., the occurrence of intense and sparse small-scale structures such as vortex sheets, filaments, and fronts. This translates into non-Gaussian Probability Distribution Functions (PDFs) of velocity and temperature gradients, as well as chemical tracer gradients. On the other hand, the atmosphere and the ocean are also known for their intermittency in large scales, with strong wings in the PDFs of the vertical velocity and temperature fields themselves. Such high vertical velocities are observed in the nocturnal planetary boundary layer;¹ this leads to strong spatial and temporal variations of the rate of kinetic energy dissipation, as measured in oceanic ridges.^{2,3} Similarly, microstructures, observed in the frontal Antarctic Circumpolar Current, are formed by quasigeostrophic eddies flowing over bottom topography.⁴ These structures are due to bathymetry, which has recently been assessed with increased accuracy.⁵ Such interactions between turbulence and stratification can affect many processes in the atmosphere and the ocean, such as rain formation⁶ or the lifetime of melting ice shelves.⁷

Large-scale intermittency is also found in high-resolution Direct Numerical Simulations (DNS) of stratified flows, with or without rotation,^{8,9} with a direct correlation to high levels of dissipation. However, isotropy is classically assumed when estimating energy dissipation of turbulent flows, from laboratory experiments to oceanic measurements, even though it has been known for a long time that small-scale isotropy recovers slowly in terms of the controlling parameter, such as in wakes, boundary layers, and pipe or shear flows.

A lack of isotropy can be associated with intermittency, as well as with the long-range interactions between large-scale coherent structures and small-scale dissipative eddies.¹⁰ In the purely rotating case, vertical Taylor columns form and, using particle image velocimetry, space-time dependent anisotropy has been shown to be important.¹¹ Spectra follow weak turbulence arguments for strong rotation,¹² and pressure acts on nonlocal interactions between strong vortices at small scales and large-scale fluctuations.¹³ In the case of pure stratification, its role on small-scale anisotropy was studied experimentally in detail.¹⁴ Spectral data and dissipation data are mostly stream-wise anisotropic because of the shear, on

top of the anisotropy induced by the vertical direction of stratification.¹⁵ The vertical integral length scale does not grow, contrary to its horizontal counterpart,¹⁶ and vertical scales are strongly intermittent.

Different components of the energy dissipation tensor have been evaluated, for purely stably stratified flows or wall turbulence, as a function of governing parameters,^{17–20} and a slow return to isotropy is found only for rather high buoyancy Reynolds numbers,¹⁷ of the order of $R_B \approx 10^3$ (see Eqs. (3)–(13) for definitions of parameters). With strong imposed shear and using anisotropic boxes, anisotropy is found to be strongest when turbulence is weakest, as expected, and anisotropic eddies in the small scales depend on the effective scale-separation between the large-scale energy-containing eddies, or the buoyancy scale for stratified flows, and the dissipative scale of the turbulence.¹⁷ Part of the difficulty in assessing the return to isotropy in either large or small scales, however, is that there is a strong coupling between scales, through the interactions of gravity waves and fine-structure shear layers,²¹ as well as in fronts.

In this context, we evaluate quantitatively the link between mixing and dissipation, anisotropy and intermittency in the presence of both rotation and stratification, and as a function of the intensity of the turbulence. This is accomplished in the framework of a large series of unforced DNS runs for the Boussinesq equations. With \mathcal{P} as the total pressure, $\mathbf{u} = \mathbf{u}_\perp + w\hat{e}_z$ as the velocity, θ as the temperature fluctuation (normalized to have dimensions of a velocity), and $\nabla \cdot \mathbf{u} = 0$ because of incompressibility, we have in the unforced case

$$\frac{\partial \mathbf{u}}{\partial t} + \boldsymbol{\omega} \times \mathbf{u} + 2\boldsymbol{\Omega} \times \mathbf{u} = -N\theta\hat{e}_z - \nabla\mathcal{P} + \nu\nabla^2\mathbf{u}, \quad (1)$$

$$\frac{\partial \theta}{\partial t} + \mathbf{u} \cdot \nabla\theta = Nw + \kappa\nabla^2\theta, \quad (2)$$

where ν is the viscosity, κ is the diffusivity, $\boldsymbol{\omega} = \nabla \times \mathbf{u}$ is the vorticity, and N is the Brunt-Väisälä frequency. Rotation, of intensity $\Omega = f/2$, and stratification are in the vertical (z) direction.

We use the pseudo-spectral Geophysical High Order Suite for Turbulence (GHOST) code with hybrid MPI/OpenMP/CUDA parallelization and linear scaling up to at least 130 000 cores.²² The GHOST-generated database considered here consists of 56 simulations on grids of 1024^3 points, as well as three at 512^3 , 12 at 256^3 , and two at 128^3 resolutions, all in a triply periodic box.^{23,24} Initial conditions for most runs are isotropic in the velocity; thus, at $t = 0$, $w/u_\perp \lesssim 1$, and we take zero temperature fluctuations so that θ develops in a dynamically consistent way. Initial conditions in quasigeostrophic (QG) equilibrium have also been considered,²³ in that case with $N/f \approx 5$, $w(t = 0) = 0$, and $\theta(t = 0) \neq 0$. The analysis of the QG set of runs, indicated in the figures by star symbols, has not introduced any major change in the conclusions,²⁴ although it displays more intermittency and anisotropy (see Figs. 4 and 5 below). Finally, with \perp referring to the horizontal direction, $k = \sqrt{|\mathbf{k}_\perp|^2 + k_z^2}$ is the isotropic wavenumber.

The dimensionless parameters of the problem are the Reynolds, Froude, Rossby, and Prandtl numbers,

$$Re = \frac{U_0 L_{int}}{\nu}, \quad Fr = \frac{U_0}{L_{int} N}, \quad Ro = \frac{U_0}{L_{int} f}, \quad Pr = \frac{\nu}{\kappa}, \quad (3)$$

where U_0 is the *rms* velocity and $L_{int} = \int [E_v(k)/k] dk / E_v$ is the isotropic integral scale, both evaluated at the peak of dissipation. For all runs, we set $Pr = 1$. The kinetic, potential, and total energies E_v , E_p , and $E_T = E_v + E_p$, of respective isotropic Fourier spectra $E_{v,p,T}(k)$, and their dissipation rates $\bar{\epsilon}_{v,p,T}$ are

$$E_v = \langle |\mathbf{u}|^2 / 2 \rangle, \quad \bar{\epsilon}_v = DE_v / Dt = \nu Z_V, \quad Z_V = \langle |\boldsymbol{\omega}|^2 \rangle, \quad (4)$$

$$E_p = \langle \theta^2 / 2 \rangle, \quad \bar{\epsilon}_p = DE_p / Dt = \kappa Z_p, \quad Z_p = \langle |\nabla\theta|^2 \rangle, \quad (5)$$

with $\bar{\epsilon}_T = \bar{\epsilon}_v + \bar{\epsilon}_p$ and where $Z_{v,p}$ are the kinetic and potential enstrophies. Spectra can also be expressed in terms of k_\perp or k_z [as in Eq. (11) below]. It may also be useful to define other derived parameters. For example, the Richardson number Ri , buoyancy Reynolds number R_B , buoyancy interaction parameter R_{IB} , and gradient Richardson number Ri_g are written as

$$Ri = (N/S)^2, \quad R_B = ReFr^2, \quad (6)$$

$$R_{IB} = \bar{\epsilon}_v / (\nu N^2), \quad Ri_g = N(N - \partial_z \theta) / S(\mathbf{x})^2, \quad (7)$$

with $S = \langle S(\mathbf{x}) \rangle = \langle \partial_z u_\perp \rangle$ representing the internal mean shear that develops in a dynamically consistent way and in the absence of imposed external shear. Ri_g is a point-wise measure of buoyancy instability; it can be negative when the vertical temperature gradient is locally larger than the (constant) Brunt-Väisälä frequency, indicative of strong local overturning. We should note here that different definitions can be found in the literature. In particular, the buoyancy Reynolds number is often expressed as²⁵ $\bar{\epsilon}_v / [\nu N^2]$, corresponding to R_{IB} here. The distinction between R_B and R_{IB} is physically important. Indeed, we can also define β as a global measure of the efficiency of kinetic energy dissipation, with respect to its dimensional evaluation $\epsilon_{D \sim U_0^3 / L_{int}}$,

$$\beta \equiv \bar{\epsilon}_v / \epsilon_D = \tau_{NL} / T_v, \quad (8)$$

$$\tau_{NL} = L_{int} / U_0, \quad T_v = E_v / \bar{\epsilon}_v. \quad (9)$$

τ_{NL} and T_v are the two characteristic times defining nonlinear transfer and energy dissipation; one can also define the wave periods as $\tau_{BV} = 2\pi/N$ and $\tau_f = 2\pi/f$. Consequently, in the intermediate regime of wave-eddy interactions, one has the following simple relationship:

$$R_{IB} = \beta R_B. \quad (10)$$

This can be justified through a dimensional argument corroborated by numerical results.²⁴ Note that, in fully developed turbulence, one has $T_v = \tau_{NL}$ and $\beta = 1$. We also showed that the characteristic times associated with the velocity and temperature and based on their respective dissipation rates, T_v and $T_p = E_p / \bar{\epsilon}_p$, vary substantially with governing parameters, being comparable in a narrow range of Froude numbers when large-scale shear layers destabilize.²⁶ The direct numerical simulations cover a wide range of parameters,^{24,26,27}

$$10^{-3} \leq Fr \leq 5.5, \quad 2.4 \leq N/f \leq 312, \quad 1600 \leq Re \leq 18\,590.$$

R_B and R_{IB} vary roughly from 10^{-2} to 10^5 , values which, at the upper end, are relevant to the ocean and atmosphere. A few purely stratified runs are considered as well.

Anisotropy has been studied extensively for a variety of flows,²⁸ and many diagnostics have been devised. Here, we concentrate on the following set, starting with the integral scale, the subscript μ representing z, \perp :

$$\frac{L_{int,\mu}}{2\pi} = \frac{\Sigma k_\mu^{-1} E_v(k_\mu)}{\Sigma E_v(k_\mu)}, \quad (11)$$

with L_{int} representing the integral scale for the isotropic case, which is in terms of isotropic wavenumber. Integral scales are known to increase with time in FDT, and it has been shown to do the same in rotating and/or stratified turbulence. This is a manifestation of the interactions between widely separated scales that feed the large-scale flow through what is known as eddy noise together with, in the rotating case in the presence of forcing, the occurrence of an inverse cascade of energy.

Other signatures of anisotropy can be obtained through the properties of the following tensors:

$$b_{ij} = \frac{\langle u_i u_j \rangle}{\langle u_k u_k \rangle} - \frac{\delta_{ij}}{3}, \quad d_{ij} = \frac{\langle \partial_k u_i \partial_k u_j \rangle}{\langle \partial_k u_m \partial_k u_m \rangle} - \frac{\delta_{ij}}{3}, \quad (12)$$

$$g_{ij} = \frac{\langle \partial_i \theta \partial_j \theta \rangle}{\langle \partial_k \theta \partial_k \theta \rangle} - \frac{\delta_{ij}}{3}, \quad v_{ij} = \frac{\langle \omega_i \omega_j \rangle}{\langle \omega_k \omega_k \rangle} - \frac{\delta_{ij}}{3}. \quad (13)$$

These tensors are equal to zero in the isotropic case. For reference, we also write the pointwise dissipation, $\epsilon_v(\mathbf{x}) = 2\nu s_{ij} s^{ij}$, where $s_{ij}(\mathbf{x}) = \frac{1}{2}(\partial_i u_j + \partial_j u_i)$ is the strain rate tensor. We define as usual the second- and third-order invariants of a tensor T_{ij} as $T_{II} = T_{ij} T_{ji}$ and $T_{III} = T_{ij} T_{jk} T_{ki}$. For the tensors above, they are denoted, respectively, $b_{II,III}$, $d_{II,III}$, $g_{II,III}$, and $v_{II,III}$ (see, for example, the work of Browne *et al.*,¹⁰ Smyth and Moum,¹⁷ Sagaut and Cambon,²⁸ and Antonia *et al.*²⁹ for details and interpretation). They refer, in particular, to the geometry of the fields (one-dimensional or 1D vs 2D, 3D, and axisymmetric, oblate or prolate). In what follows, all anisotropy tensors and their invariants are computed from a snapshot of the data cube at the peak of total enstrophy $Z_T = \langle |\boldsymbol{\omega}|^2 + |\nabla\theta|^2 \rangle$ (and thus, at the peak of dissipation ϵ_T) for each run, as are all PDFs and quantities associated with buoyancy flux, e.g., Γ_f defined in Sec. II. All other quantities that are plotted are computed based on spectra that are averaged in time over the peak in enstrophy. Specifically, the chosen time intervals, different for different runs, are taken so that the variation of the total enstrophy in each case is no more than 2.5% from its peak value when the turbulence is fully developed. This ensures a

lack of correlation between data points within the parametric study. Note that most of the symbols used throughout the paper, together with their definitions, are provided for convenience in [Appendix, Table I](#).

II. AT THE THRESHOLD OF SHEAR INSTABILITIES

Rotating stratified turbulence (RST) consists of an ensemble of interacting inertia-gravity waves and (nonlinear) eddies. It can be classified into three regimes, I, II, and III, with dominance of waves in I for a small Froude number (and small R_{IB}) and dominance of eddies in III for high R_{IB} : then, the waves play a secondary role and dissipation recovers its fully developed turbulence isotropic limit $\bar{\epsilon}_D$, within a factor of order unity.³⁰ In the intermediate regime (regime II), one finds (i) $\beta \sim Fr$, as required by weak turbulence arguments; this is the first central result by Pouquet *et al.*,²⁴ together with the following two other laws: (ii) kinetic and potential energies are proportional (but not equal), with no dependence on governing parameters in regime II where waves and nonlinear eddies strongly interact, and (iii) similarly for the ratio of vertical to total kinetic energy, E_z/E_v .

With these three constitutive laws [(i)–(iii)], one can recover and establish a large number of scaling relationships, such as for the ratio of characteristic length scales,²⁴ or for the mixing efficiency defined as

$$\Gamma_f \equiv B_f / \bar{\epsilon}_v, \quad B_f = N \langle w \theta \rangle, \quad (14)$$

with B_f being the buoyancy flux. One finds $\Gamma_f \sim R_B^{-1} \sim Fr^{-2}$ in regimes I and II, and $\sim R_B^{-1/2} \sim Fr^{-1}$ in regime III. Such scalings, predicted from simple physical arguments in Ref. 24, have been observed at high R_{IB} , for example, in oceanic data.³¹ Defining $\Gamma_* \equiv \bar{\epsilon}_p / \bar{\epsilon}_v$ as the reduced mixing efficiency provides another simple measure of irreversible mixing by looking at how much dissipation occurs in the potential and kinetic energy, respectively. It is easily shown using the laws given above that, for the saturated regime III, $\Gamma_* \sim Fr^{-2}$ since the Ellison scale $L_{Ell} = 2\pi\theta_{rms}/N$ becomes comparable to L_{int} in that case (see Fig. 6 in that paper). These scaling laws extend smoothly to the purely stratified flows we have analyzed, where, for regime II, the reduced mixing efficiency was found to vary linearly with the Froude number.⁹ These results are also compatible with other results obtained for that case.^{19,20,25,32,33}

We thus begin our investigation by examining mixing and dissipation. We show in [Fig. 1](#) the dissipation efficiency $\beta = \bar{\epsilon}_v / \epsilon_D$ as a

FIG. 1. Left: Variation with the Richardson number of the kinetic energy dissipation efficiency β . The Roman numerals at the bottom delineate the three regimes of rotating stratified turbulence.²⁴ Right: Variation with the buoyancy interaction parameter R_B of the mixing efficiency Γ_f defined in Eq. (14). Colored symbols indicate Rossby number ranges (see the inset).

function of Richardson number. Unless specified otherwise, data are binned in the Rossby number [refer to the legend in Fig. 1 (left)], as in most subsequent scatter plots, with roughly the same number of runs in each bin. For runs initialized with random isotropic conditions, the color *and* symbol of a given data point both indicate which Rossby number bin it resides in. Star symbols are used for quasi-geostrophic initial conditions, with a balance between the pressure gradient, Coriolis force, and gravity, and the color alone indicates the bin range it belongs to. For all scatter plots, the size of a symbol is proportional to the viscosity of the run, with the smallest symbols denoting runs on grids of 1024^3 points and higher Reynolds numbers, and the two largest symbols denoting the two runs on grids of 128^3 points at the lowest Re .

Note in the plot of $\beta(Ri)$ the presence of an inflection point for $Ri \lesssim 1/4$, and the two plateaux starting at $Ri \approx 10^{-2}$ and ≈ 10 with an approximate scaling $\beta \sim Ri^{-1/2}$ in the intermediate regime, consistent with $\beta \sim Fr$, as found before.²⁴ As stated earlier, this defines the three regimes of rotating stratified turbulence, I, II and III, in a similar fashion as for the case of purely stratified turbulence.²⁵

The mixing efficiency Γ_f is plotted in Fig. 1 (right) as a function of buoyancy interaction parameter R_{IB} . The three data points with $R_{IB} \gtrsim 10^4$ have Froude numbers above unity. It also follows approximately two scaling laws. It can become singular in the quasi-absence of kinetic energy dissipation (when measured in terms of buoyancy flux), and indeed, Γ_f takes high values for the runs at low Fr . Its slower decay with R_{IB} for strongly turbulent flows starts at a pivotal value of $R_{IB} \approx 1$, a threshold which will be present in most of the data analyzed herein. The decay of Γ_f to low values is inexorable in the absence of forcing and with zero initial conditions

in the temperature field, which, at high R_{IB} , becomes decoupled from the velocity and evolves in time in a way close to that of a passive scalar.

Figures 2(a)–2(c) display the variation with time of the kinetic energy and enstrophy, E_v and Z_v , where the time is expressed in units of turn-over time, τ_{NL} , defined in Eq. (9). The specific runs are computed on grids of 1024^3 points. There is roughly a factor of 10 in Froude number from regimes I to II and from II to III; specifically, we have run 5, with $Fr \approx 0.007$, $N/f \approx 31$, $Re \approx 14000$, $\mathcal{R}_B \approx 0.75$ in regime I; run 32, with $Fr \approx 0.07$, $N/f \approx 42$, $Re \approx 12200$, $\mathcal{R}_B \approx 65$ in regime II; and run 58, with $Fr \approx 0.89$, $N/f \approx 2.5$, $Re \approx 4700$, $\mathcal{R}_B \approx 3760$ in the third regime.^{23,24} Note the different scales on both axes, and the different ranges of values for enstrophy in the three regimes: there is more enstrophy (and hence more dissipation) as we move from regime I to regime III. There are fast oscillations in the first regime [Fig. 2(a)]. They are a signature of the fast exchanges (compared to the turn-over time) of energy between the kinetic and potential modes. In regime II [Fig. 2(b)], the oscillations are slower and become more complex once the maximum of enstrophy is reached and the flow is a superposition of nonlinearly interactive modes. Finally, the higher enstrophy values in the last regime [Fig. 2(c)] are related to strong small-scale dissipative structures. The maximum of kinetic enstrophy (and thus of kinetic energy dissipation) is reached at a later time in regime I than in the other two regimes, corresponding to a slower development of small scales through weak nonlinear mode coupling. Also, as expected, the energy decays faster as we approach the fully turbulent regime. Similar results hold for the potential energy and its dissipation (not shown).

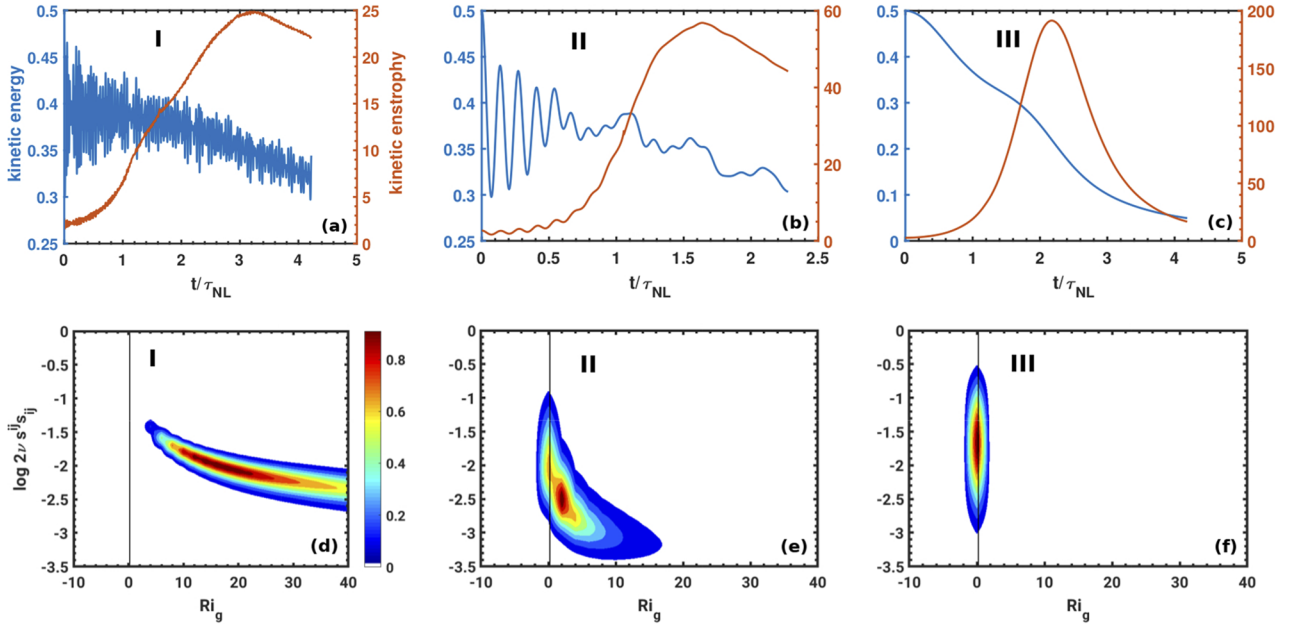


FIG. 2. [(a)–(c)] Temporal variations, in units of turn-over time, of kinetic energy (left, blue axis in each plot) and of kinetic enstrophy $Z_v = \langle |\omega|^2 \rangle$ (right, red axis in each plot). All runs are performed on grids of 1024^3 points and are in one of the three regimes identified in Fig. 1 (see text for parameters): I (a), II (b), and III (c). [(d)–(f)] Joint PDFs of point-wise kinetic energy dissipation $\epsilon_v(\mathbf{x})$ and gradient Richardson number $Ri_g(\mathbf{x})$ for the same three runs as above. $Ri_g = 1/4$ is indicated by the thin vertical lines. All plots use the same color bar given at the left.

Joint PDFs of the pointwise gradient Richardson number and kinetic energy dissipation, for the same runs as in the top panels, are shown in Figs. 2(d)–2(f). The threshold of shear instability, $Ri_g = 1/4$, is indicated in all three plots by a thin vertical line. For regime II [Fig. 2(e)], most points in the flow are close to (but still slightly above) the threshold, $Ri_g \gtrsim 1$. The pointwise kinetic energy dissipation is centered on $\approx 3 \times 10^{-3}$ but covers locally a range of values almost two orders of magnitude wide for $Ri_g \approx 1$. For runs in regime I [Fig. 2(d)], no data point reaches $Ri_g = 1$, and rather dissipation values are found in a narrow band extending to high Ri_g . On the other hand, in the opposite case of strongly turbulent flows [regime III in Fig. 2(f)], the bulge of points around $Ri_g \approx 1/4$ is much narrower with a flow almost everywhere at the brink of linear instability, reaching higher values of local dissipation, and with a larger extension in its local values, over 2.5 orders of magnitude; this can be seen as being indicative of intermittent behavior, as we shall analyze below in Fig. 4. This high number of data points, for a given setup, with local gradient Richardson numbers close to $1/4$ (or zero for convective instability) has been noted before by several authors. For example, an equivalent result based on an earlier analysis of oceanic data³⁴ (see Fig. 15) shows that in that case, most of the points are centered at $Ri_g \approx 0.4$, with also roughly four orders of magnitude in the variation of the local energy dissipation rate. Such a high density of values for $Ri_g \approx 1/4$ has recently been interpreted as a manifestation of self-organized criticality,³⁵ with flow destabilization occurring in a wide range of intensity displaying power-law behavior, as analyzed on observations of oceanic microstructures.

We now focus on the anisotropy of these flows. Large-scale anisotropy can be measured by the ratio $L_{int,z}/L_{int,\perp}$. As shown in Fig. 3(a), it increases with R_{IB} at a slow rate, starting at $R_{IB} \approx 1$ before settling sharply to a value close to unity for high $R_{IB} \approx 10^3$. At small R_{IB} , the larger vertical integral scale (with respect to its horizontal counterpart), indicative of a lesser anisotropy for strong rotation and stratification (blue triangles), can be attributed to initial conditions that are isotropic together with, in that range, weak nonlinear coupling. Note that, at a given R_{IB} , vertical scales are almost a factor of 2 larger for stronger rotation, with a clear clustering of points with $Ro \leq 0.3$ (blue triangles) at intermediate values of R_{IB} . This can be associated with a stronger inverse energy transfer due to rotation, although an inverse energy cascade is not directly observed in the absence of forcing, but can appear, for long times, as an envelope to the temporal decay behavior of a turbulent flow.³⁶

In Figs. 3(b) and 3(c) are shown the second invariants, $d_{II}^{1/2}$ and $v_{II}^{1/2}$ of the velocity gradient and vorticity tensors [see Eq. (13) for definitions], again as functions of R_{IB} . While anisotropy expressed in terms of $d_{II}^{1/2}$ seems to show an approximate power law decrease toward isotropy (with power law index $-1/3$), in $v_{II}^{1/2}$ the three regimes of mixing are again visible. In the latter, a sharp transition is observed at $R_{IB} \gtrsim 100$. In terms of Froude number, the intermediate regime is bounded by $Fr \in [0.03, 0.2]$, and in terms of R_B , it is bounded by $R_B \in [10, 300]$. Note that the Fr bounds encompass that for which the large-scale intermittency is strongest in the case of purely stratified forced flows, as measured by the kurtosis of the vertical Lagrangian velocity⁹ (see also Fig. 4). Note also that, for the highest values of the buoyancy interaction parameter, we have a small $d_{II}^{1/2} \approx 10^{-3}$, whereas in terms of the vorticity tensor, the tendency toward isotropy is much slower, with a lowest value of order 10^{-1} , indicative of vorticity structures that retain a signature of the imposed anisotropy.

This variable anisotropy associated with strong mixing properties is also accompanied by marked intermittency, at small scales and also in large scales. We first analyze in Fig. 4 the PDFs of the vertical temperature gradients, either normalized (a, left) or without normalization (b, middle). Both are binned in $N/f = Ro/Fr$, and at the left, the dotted line represents the corresponding Gaussian distribution. As expected, the PDFs are non-Gaussian for all parameters, with wings the intensity of which varies somewhat with N/f . We note however that such wings are present from purely stratified flows to strongly rotating (and stratified) flows with $Ro \leq 0.3$. Gradients favor small scales, but large scales are intermittent as well, as found already for purely stratified flows,⁸ at least for an interval of parameters.⁹ As an example of such large-scale intermittency, we plot at right (c) the kurtosis of the vertical component of the Eulerian velocity, w , at the peak of dissipation, with the kurtosis defined as $K_w = \langle w^4 \rangle / \langle w^2 \rangle^2$. When considering only the runs with isotropic initial conditions, the increase in K_w is rather smooth and with a peak at $R_{IB} \approx \mathcal{O}(10)$ of $K_w \lesssim 4$. What is particularly striking, however, is the “bursty” behavior seen in the runs with QG initial conditions (indicated by stars) with a peak of $K_w \approx 7.5$ at $R_{IB} \gtrsim 1$, or at $Fr \approx 0.07$, in good agreement with what is found for forced flows.⁹ The high values we see in K_w are comparable to those observed in the atmosphere.^{1,37} Note however that the peaks in K_w , K_θ are intermittent in time,⁹ whereas our analysis is done at a fixed time close to the maximum

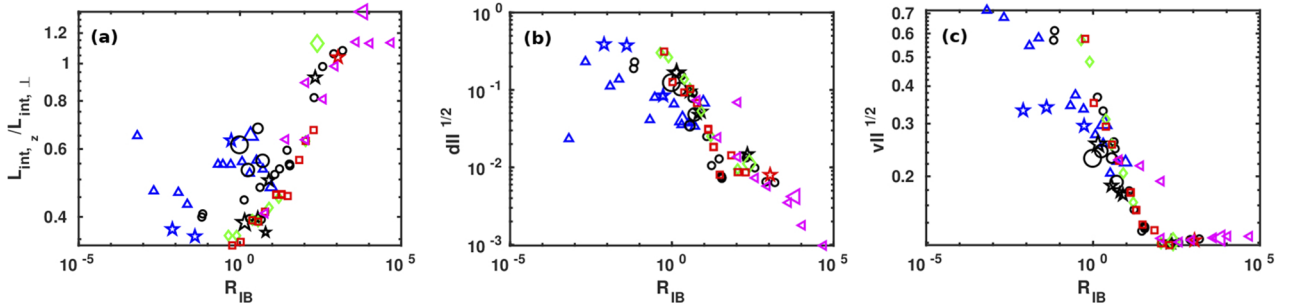


FIG. 3. As a function of buoyancy interaction parameter $R_{IB} = \bar{\epsilon}_v / [\nu N^2]$, we plot (a) the ratio of vertical to horizontal integral scales [see Eq. (11)], (b) $d_{II}^{1/2}$, and (c) $v_{II}^{1/2}$ [see Eq. (13) for definitions of second tensor invariants for the velocity and vorticity, $d_{II}^{1/2}$ and $v_{II}^{1/2}$]. Binning is in the Rossby number.

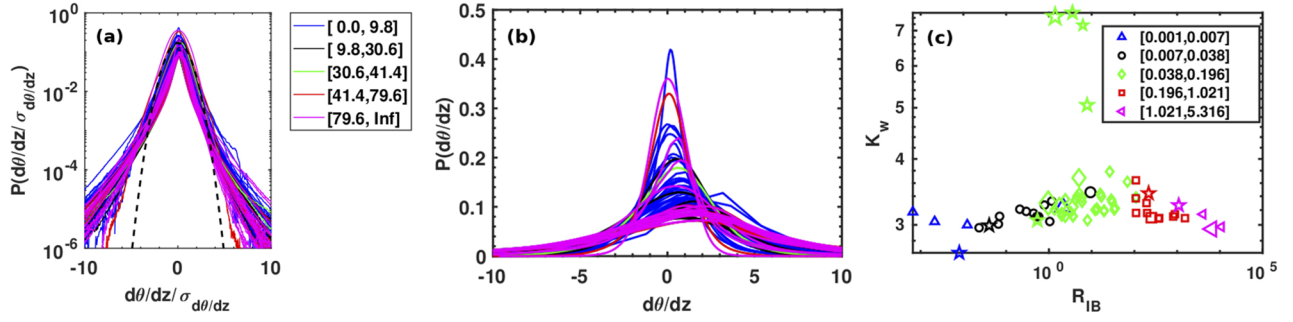


FIG. 4. (a) Normalized PDFs of $\partial_z \theta$ with binning in Nlf (see legend). The dotted black line is the corresponding Gaussian distribution. (b) The same PDFs without the normalization. (c) Kurtosis of vertical velocity as a function of R_{IB} , with binning in the Froude number as indicated in the legend.

dissipation of the flows, in order to maximize the effective Reynolds number of each run.

The behavior of the QG runs with significantly higher kurtosis is probably due to the fact that their initial conditions are

two-dimensional and with $w = 0$. In such a case, for a small Froude number and at least for small times, the advection term leads to smooth fields, and the flow has to develop strong vertical excitation characteristics of stratified turbulence, through local

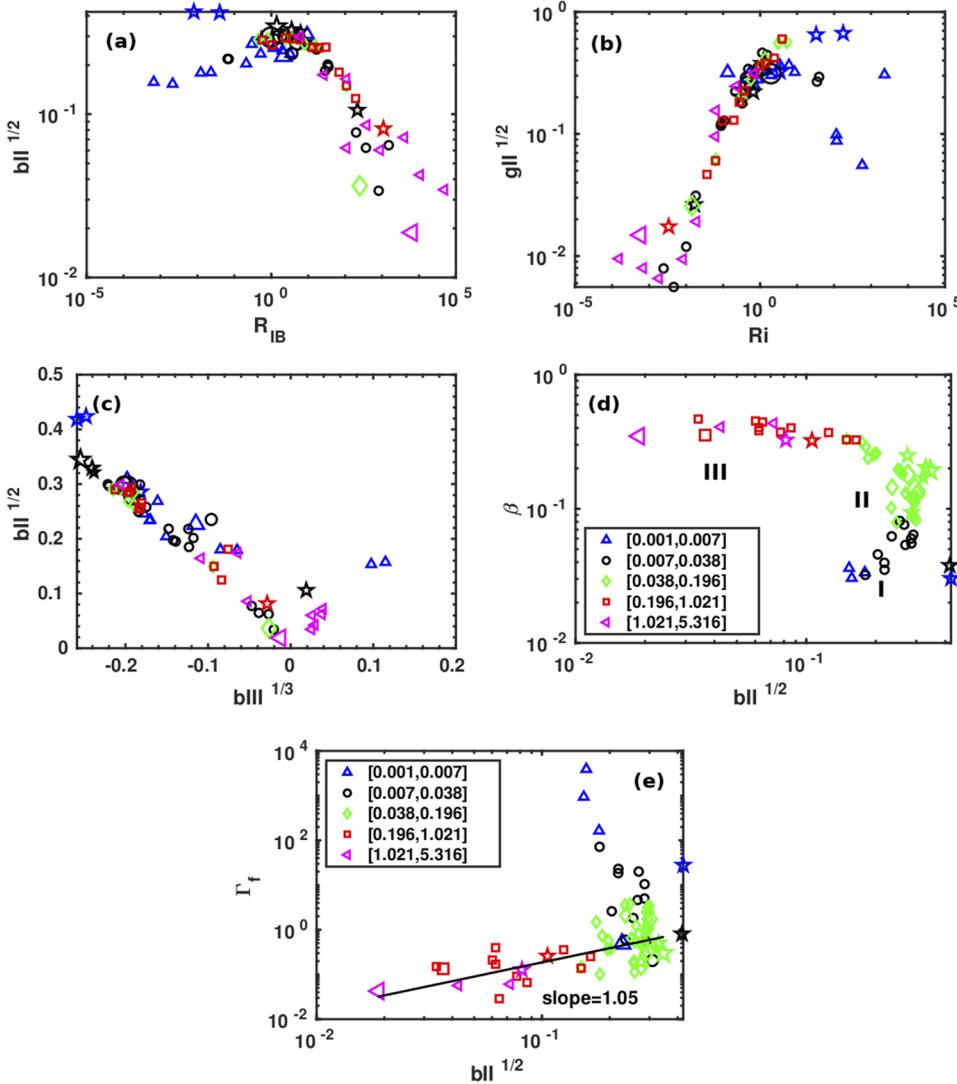


FIG. 5. Velocity and temperature invariants defined in Eq. (13): (a) $b_{II}^{1/2}$ vs R_{IB} , (b) $g_{II}^{1/2}$ vs Ri , (c) $b_{II}^{1/2}$ vs $b_{III}^{1/3}$, and (d) β vs $b_{II}^{1/2}$, showing the three regimes as in Fig. 1. In (e) is given the mixing efficiency Γ_f vs $b_{II}^{1/2}$, with a best-fit reference line for $Fr > 0.05$. In (a)–(c), color binning is done in terms of the Rossby number (see the inset of Fig. 1), whereas in (d) and (e) it is in terms of Fr .

instabilities, in order to catch up with energy dissipation and with emerging tendencies toward isotropy in small scales. The temperature (not shown) displays for most runs a relatively flat kurtosis at close to its Gaussian value, $K_\theta^{(G)} \approx 3$, but still exhibits a rather sharp increase to $K_\theta \gtrsim 4.2$ in the QG-initialized runs at $R_{IB} \approx 1$, as well as for smaller values of the Froude number and buoyancy interaction parameter R_{IB} .

We provide in Fig. 5 the parametric variations for some of the velocity- and temperature-related anisotropy tensor invariants defined in Eq. (13). Figures 5(a) and 5(b) show b_{II} as a function of R_{IB} and g_{II} as a function of Ri , respectively. Both have a peak at $R_{IB} \approx 1$, $Ri \approx 1$ (corresponding also to $Fr \approx 0.075$, $R_B \approx 10$, not shown); however, we note that $g_{II,III}$ have a maxima for slightly smaller values of Fr . The final transition to a plateau approaching isotropic values, seen in Fig. 5(a), occurs for high $R_{IB} \approx 10^3$, as advocated on the basis of oceanic and estuary measurements³⁸ or from DNS.^{17,20}

Having scaled nonlinearly both the second and third invariants of tensors in order for them to have the same physical dimension, we find that third invariants have similar scaling with control parameters, except that they can and do become negative, in ways comparable to what is found for purely stratified flows.¹⁷ We illustrate this in Fig. 5(c) in a scatter plot of the second and third invariants of b_{ij} that, to a large degree, fills in Fig. 6 of Ref. 17 for $b_{II}^{1/2} < 0.2$; it highlights the fact that at the peak of enstrophy, the majority of our runs are dominated by oblate axisymmetric structures, in the form of sheets. This is complementary to what is performed by using many temporal snapshots, when one can probe more of the permissible $b_{II}-b_{III}$ domain.¹⁷

We do note that there are two straggler points at high b_{II} , g_{II} , and low negative b_{III} , and in v_{II} as seen in Fig. 3(c). These runs, indicated by blue stars, have quasigeostrophic initial conditions and are at low Froude, Rossby, and buoyancy Reynolds numbers ($R_B \lesssim 1$); specifically, they are²⁴ runs Q9 and Q10 (see their Table 2). Again, the quasi-two-dimensional nature of such flows at the peak of enstrophy is confirmed in Fig. 5(c), which places these QG-initialized runs on the upper left branch. This indicates that these flows are dominated by quasi-two-dimensional sheets¹⁷ (see, e.g., their Fig. 6). Indeed, the high anisotropy observed in the vicinity of $R_B \approx 1$, $R_{IB} \approx 1$, $Fr \approx 0.07$ in Fig. 3(c) corresponds to two-dimensional structures in the form of shear layers with strong quasivertical gradients at low Fr and which eventually roll-up as they become unstable.

Figure 5(d) shows the dependence of the kinetic energy dissipation efficiency, β , on the second invariant of the velocity anisotropy tensor, this time with binning in Fr . The figure serves to complement both Fig. 1(c) of Ref. 24 and Fig. 1 (right), illustrating behavior in the three RST regimes, where β is low at reasonably high measures of (large-scale) anisotropy (as measured by b_{ij}) in regime I, approaches its highest value at largely constant $b_{II}^{1/2}$ in regime II, and as anisotropy begins to diminish at the end of regime II, remains essentially constant in regime III, as the anisotropy continues to decrease with decreasing stratification.

Finally, in order to render more explicitly the correlation between mixing and anisotropy, we show in Fig. 5(e) the mixing efficiency Γ_f , displayed against $b_{II}^{1/2}$, again with binning in the Froude number. One observes an approximate power law increase in mixing efficiency as anisotropy grows with stratification, from large to

moderate Fr , with a best fit slope of ≈ 1 . Using the definitions for β and Γ_f in terms of the buoyancy flux, we can write $\Gamma_f = [\beta Fr]^{-1} \langle w\theta \rangle / \langle u^2 \rangle$. Noting again that in regime III, β is independent of anisotropy [Fig. 5(d)] and that b_{zz} is remarkably linear in (indeed, nearly equal to) $b_{II}^{1/2}$ for all runs (not shown), the power law dependence of Γ_f on $b_{II}^{1/2}$ mainly results from the increasingly passive nature of the scalar in transitioning from regime II to regime III and continuing to larger Fr . There is also an abrupt increase in Γ_f in the smallest Fr range, corresponding to regime I with negligible kinetic energy dissipation. The transitory regime (green diamonds) in the vicinity of the peak of vertical velocity kurtosis also corresponds to maximum b_{II} , i.e., maximum anisotropy, together with mixing efficiency of order unity. The accumulation of points for Froude numbers in the intermediate range of values has large b_{II} and a mixing efficiency around unity, with quasibalanced vertical buoyancy flux and kinetic energy dissipation.

III. CONCLUSION AND DISCUSSION

We have shown in this paper that, in rotating stratified turbulence, a sharp increase in dissipation and mixing efficiency is associated, in an intermediate regime of parameters, with large-scale anisotropy, as seen in the velocity tensor b_{ij} , and large-scale intermittency, as observed in the vertical velocity through its kurtosis. The return to isotropy is slow and takes place mostly for buoyancy interaction parameters R_{IB} larger than $\approx 10^3$. The temporal persistence of anisotropic structures at a given Froude number could be related to the slow decay of energy in the presence of waves, particularly when helicity is strong.³⁹ Furthermore, rotation plays a role in large scales, with a larger vertical integral scale at a given Froude number for small Rossby numbers [see Fig. 3(a)]. The return to large-scale isotropy, as measured by $L_z/L_\perp \approx 1$, is very sharp. These results evoke threshold behavior and avalanche dynamics, as analyzed for numerous physical systems^{40–43} in the context of the solar wind and as found as well recently in observational oceanic data.³⁵

In order to determine whether a given system is undergoing self-organized criticality (SOC) in the form of so-called avalanches, and if so what SOC class the system belongs to, one needs to resort to spatiotemporal analysis, although proxies are possible, such as using static snapshots of dissipative structures and applying the law of probability conservation.⁴¹ Furthermore, different conclusions may be drawn whether one examines structures in the inertial range of turbulent flows or whether one is in the dissipative range.⁴¹ Perhaps, localized Kelvin-Helmholtz overturning vortices merge into larger regions, as a reflection of nonlocality of interactions in these flows, together with sweeping of small eddies by large-scale ones, close to the linear instability for $Ri_g = 1/4$, and leading to rare large-amplitude dissipative (avalanche) events. In that context, long-time dynamics, in the presence of forcing, should be investigated to see whether correlations emerge. A threshold analysis could be performed in these flows in terms of the number of excited sites, say above a local dissipation rate $\bar{\epsilon}_c$, as a function of a control parameter, likely the local gradient Richardson number. Temporal dynamics should also be analyzed in terms of life-time of overturning structures, as performed classically, for example, for pipe flows.^{44,45}

The burstiness of these rotating stratified flows is accompanied by a turbulence collapse. This takes place once the energy has

been dissipated at a rate close to that of homogeneous isotropic turbulence. However, we note that this rate has been found to be dependent on the ratio of the wave period controlling the waves to the turn-over time (in other words, the Froude number), in an intermediate regime of parameters.²⁴ This type of behavior has been studied, e.g., for shear flows, emphasizing both the interscale interactions between large and small eddies with rather similar statistics⁴⁶ and the importance of sharp edges in frontal dynamics.⁴⁷ This has been analyzed in the laboratory at the onset of instabilities including for Taylor-Couette flows or for pipe flows,^{45,48} and it may be related to frontal dynamics observed in the atmosphere and ocean,^{49,50} given the tendencies of such flows to be, at least in the idealized dynamical setting studied herein, at the margin of such instabilities.

Recent observations,³⁵ modeling,⁴⁹ and numerous DNS indicate that indeed the gradient Richardson number resides mainly around its classical threshold for linear instability ($\approx 1/4$), as also observed in our results, exhibiting a strong correlation with dissipation. In that light, it may be noted that the range of parameters for the mixing efficiency to be comparable to its canonical value observed in oceanic data is close to the instability threshold: $\Gamma_f \approx 0.2$ for $0.02 \lesssim Fr \lesssim 0.1$. Similarly, the kurtosis of the temperature and vertical velocity $K_{\theta,w}$ are high⁹ in a narrow window around $0.07 \leq Fr \leq 0.1$. As a specific example of marginal instability behavior in the framework of a classical model of turbulence^{51,52} extended to the stratified case, it can be shown⁵³ that the flow remains close to the stable manifold of a reduced system of equations governing the temporal evolution of specific field gradients, involving, in particular, the vertically sheared horizontal flows through the second and third invariants of the velocity gradient matrix and a cross-correlation velocity-temperature gradient tensor.

The link between localized intermittency, anisotropy, and dissipation is also found in fully developed turbulence, in the form of strong vortex filaments, non-Gaussianity of velocity gradients, and localized dissipative events. It has also been shown that a Kolmogorov spectrum $E_v(k) \sim k^{-5/3}$ can still be observed when the small scales are anisotropic.⁵⁴ The new element in rotating stratified flows is what the wave dynamics brings about, namely, a fluid in a state of marginal instability, almost everywhere close to the threshold of linear instability in terms of $Ri_g \approx 1/4$. It is already known that in magnetohydrodynamics (MHD), when coupling the velocity to a magnetic field leading to the propagation of Alfvén waves, there is stronger small-scale intermittency than for FDT, as found in models of MHD,^{55,56} in DNS,^{57,58} as well as in observations of the solar wind.⁵⁹ In RST, the added feature is having intermittency in the vertical component of the velocity and temperature fluctuations themselves, thus at large scale, as found in many observations in the atmosphere and in climatology as well,^{60,61} and limited to a narrow range of parameters⁹ centered on the marginal instability threshold. Thus, not only does this interplay between waves and nonlinear eddies not destroy these characteristic features of turbulent flows, but in fact it acts in concert with them and can rather enhance them as well.

The large database we use is at a relatively constant Reynolds number, $Re \approx 10^4$, and thus, an analysis of the variation of anisotropy with Re for fixed rotation and stratification remains to be done, in the spirit of earlier pioneering studies^{62,63} for fluids. Also, scale by scale anisotropy might be best studied with Fourier spectra. This will

be accomplished in the future, together with a study of the role of forcing.

This paper is centered on a large parametric study of rotating stratified turbulence. Each flow taken individually is strongly intermittent in space and thus presents zones that are active as well as zones that are quiescent. It was proposed recently to partition a given flow in such zones, with strong layers delimiting such patches,⁶⁴ depending on the buoyancy interaction parameter R_{IB} , and with threshold values, of roughly 1, 10, and 100. The intermediate range corresponds, in our DNS runs, to the peak of anisotropy and intermittency together with mixing efficiency being close to its canonical value, $\Gamma_f \approx 0.2$. In this regard, it will be of interest to perform such a local study for a few given runs of our database in the three regimes.

Many other extensions of this work can be envisaged. For example, one could perform a wavelet decomposition to examine the scale-by-scale anisotropy and intermittency in such flows.⁶⁵ Moreover, kinetic helicity, the correlation between velocity and vorticity, is created by turbulence in rotating stratified flows.^{66,67} It is the first breaker of isotropy since flow statistics depend only on the modulus of wavenumbers, but two defining functions (energy and helicity density) are necessary to fully describe the dynamics. In FDT, helicity is slaved to the energy in the sense that $H_v(k)/E_v(k) \sim 1/k$, i.e., isotropy is recovered in small scales at the rate $1/k$. In the stratified case, its scale distribution changes with Brunt-Väisälä frequency,³⁹ as measured for example in the planetary boundary layer (PBL),⁶⁸ and it undergoes a direct cascade to small scales, while energy goes to large scales in the presence of strong rotation and forcing.⁶⁹ What role helicity and the nonlinear part of potential vorticity, namely, $\omega \cdot \nabla \theta$, will play in the fast destabilization of shear layers, their intermittency, anisotropy, and criticality are topics for future work.

We conclude by noting that a deeper understanding of the structure of small-scale rotating stratified turbulence, and of the nonlocal interactions between small scales and large scales, will allow for better modeling in weather and climate codes. Many models of anisotropic flows have been proposed⁷⁰⁻⁷³ including artificial neural networks. They extend isotropic formulations for kinetic energy dissipation by adding several off-diagonal terms, and assuming (or not) isotropy in the orthogonal plane,^{14,15} including for two-point closures.²⁸ This modeling strategy has already been found useful in models of turbulent mixing in oceanic simulations.^{74,75}

ACKNOWLEDGMENTS

The runs analyzed in this paper have been performed using an ASD allocation at NCAR, supplemented by a large amount of background time, for both of which we are thankful. NCAR is funded by the National Science Foundation. R.M. acknowledges support from the program PALSE (Programme Avenir Lyon Saint-Etienne) of the University of Lyon, in the framework of the program Investissements d’Avenir (Grant No. ANR-11-IDEX-0007), from the Inge’LySE (Lyon-Saint_Etienne) and from the project “DisET” (Grant No. ANR-17-CE30-0003). Support for A.P. from LASP, and, in particular, from Bob Ergun, is gratefully acknowledged.

APPENDIX: SYMBOL DEFINITIONS

We put together in the following table, for convenience, the various symbols that are used in the paper, with their definitions and names.

TABLE I. List of most symbols used in the paper, with definitions and names (refer as well to the main text). One can also define perpendicular and vertical integral scales, when using the spectra based on perpendicular and vertical wavevectors (see main text). Also note that, in the third regime of rotating stratified turbulence, $R_B = R_{IB}$ because now $\bar{\epsilon}_v = \epsilon_D$. For all entries, a boldface type indicates a vector quantity.

Symbol	Definition	Description	Remarks
\mathbf{u}		Velocity fields of components $[u_\perp, w]$	
$\boldsymbol{\omega}$	$\boldsymbol{\omega} = \nabla \times \mathbf{u}$	Vorticity field	
S	$\langle \partial_z u_\perp \rangle$	Internal mean vertical shear	Of local density $S(\mathbf{x})$
θ		Temperature fluctuations	
P		Pressure	
\mathbf{k}		Wavevector of modulus $k = [\mathbf{k}_\perp^2 + k_z^2]^{1/2}$	
U_0		Characteristic velocity	
$E_v(k)$	$\int E_v(k) dk = \langle \mathbf{u} ^2 / 2 \rangle$	Isotropic kinetic energy spectrum	
L_{int}	$2\pi \int [E_v(k)/k] dk / E_v$	Integral scale	
$E_p(k)$	$\int E_p(k) dk = \langle \theta^2 / 2 \rangle$	Isotropic potential energy spectrum	Total energy $E_T = E_v + E_p$
N		Brunt-Väisälä frequency	
f	2Ω	Rotation frequency	Ω : imposed rotation rate
ν		Viscosity	
κ		Diffusivity	
Z_v	$\langle \boldsymbol{\omega} ^2 \rangle$	Kinetic enstrophy	
Z_p	$\langle \nabla \theta ^2 \rangle$	Potential enstrophy	Total enstrophy $Z_T = Z_v + Z_p$
$\bar{\epsilon}_v$	νZ_v	Mean kinetic energy dissipation	
$\bar{\epsilon}_p$	κZ_p	Mean potential energy dissipation	Total dissipation $\bar{\epsilon}_T = \bar{\epsilon}_v + \bar{\epsilon}_p$
ϵ_D	U_0^3 / L_{int}	Dimensional kinetic energy dissipation	
$s_{ij}(\mathbf{x})$	$(\partial_i u_j + \partial_j u_i) / 2$	Pointwise strain rate tensor	$\epsilon_v(\mathbf{x}) = 2\nu s_{ij}(\mathbf{x}) s^{ij}(\mathbf{x})$
η	$[\nu^3 / \bar{\epsilon}_v]^{1/4}$	Kolmogorov (dissipation) scale	
τ_{NL}	L_{int} / U_0	Dimensional eddy turn-over time	
T_v	$E_v / \bar{\epsilon}_v$	Effective transfer and dissipation time	For the kinetic energy
T_p	$E_p / \bar{\epsilon}_p$	Effective transfer and dissipation time	For the potential energy
Re	$U_0 L_{int} / \nu$	Reynolds number	Four governing parameters
Fr	$U_0 / (L_{int} N)$	Froude number	
Ro	$U_0 / (L_{int} f)$	Rossby number	
Pr	ν / κ	Prandtl number	Equal to unity for all runs
R_B	$Re Fr^2$	Buoyancy Reynolds number	Four derived parameters
R_{IB}	$\bar{\epsilon}_v / (\nu N^2)$	Buoyancy interaction parameter	At times called buoyancy parameter ²⁵
Ri	N^2 / S^2	Richardson number	
Ri_g	$N(N - \partial_z \theta) / S(\mathbf{x})^2$	Pointwise gradient Richardson number	Close to instability threshold
B_f	$\langle w\theta \rangle$	Vertical buoyancy flux	
Γ_f	$B_f / \bar{\epsilon}_v$	Mixing efficiency	
Γ_*	$\bar{\epsilon}_p / \bar{\epsilon}_v$	Reduced mixing efficiency	
ℓ_{Oz}	$2\pi [\bar{\epsilon}_v / (N^3)]^{1/2}$	Ozmidov scale	$\ell_{Oz} / \eta \sim R_{IB}^{3/4}$
L_{Ell}	$2\pi \theta_{rms} / N$	Ellison scale	$L_{Ell} / L_{int} \sim Fr$ in regime II
β	$\bar{\epsilon}_v / \epsilon_D$	Dissipation efficiency	$\beta \sim Fr$ in regime II
		β quantifies the changing role of the waves	See the work of Pouquet <i>et al.</i> ²⁴
b_{ij}	$\langle u_i u_j \rangle / \langle u_k u_k \rangle - \delta_{ij} / 3$	Velocity tensor, zero for isotropy	Invariants b_{II}, b_{III}
d_{ij}	$\langle \partial_k u_i \partial_k u_j \rangle / \langle \partial_k u_m \partial_k u_m \rangle - \delta_{ij} / 3$	Velocity gradient tensor, zero for isotropy	Invariants d_{II}, d_{III}
v_{ij}	$\langle \omega_i \omega_j \rangle / \langle \omega_k \omega_k \rangle - \delta_{ij} / 3$	Vorticity tensor, zero for isotropy	Invariants v_{II}, v_{III}
g_{ij}	$\langle \partial_i \theta \partial_j \theta \rangle / \langle \partial_k \theta \partial_k \theta \rangle - \delta_{ij} / 3$	Temperature gradient tensor, 0 for isotropy	Invariants g_{II}, g_{III}
K_w	$\langle w^4 \rangle / \langle w^2 \rangle^2$	Kurtosis (of vertical velocity)	3 for a Gaussian PDF

REFERENCES

- ¹D. H. Lenschow, M. Lothon, S. D. Mayor, P. P. Sullivan, and G. Canut, "A comparison of higher-order vertical velocity moments in the convective boundary layer from lidar with in situ measurements and large-eddy simulation," *Boundary-Layer Metrol.* **143**, 107 (2012).
- ²J. M. Klymak, R. Pinkel, and L. Rainville, "Direct breaking of the internal tide near topography: Kaena Ridge, Hawaii," *J. Phys. Oceanogr.* **38**, 380 (2008).
- ³H. van Haren and L. Gostiaux, "Convective mixing by internal waves in the Puerto Rico Trench," *J. Mar. Res.* **74**, 161 (2016).
- ⁴K. Zheng and M. Nikurashin, "Downstream propagation and remote dissipation of internal waves in the southern ocean," *J. Phys. Oceanogr.* **49**, 1873 (2019).
- ⁵S. Kar and A. Guha, "Ocean bathymetry reconstruction from surface data using hydraulics theory," *Phys. Fluids* **30**, 121701 (2018).
- ⁶R. Shaw and S. P. Oncley, "Acceleration intermittency and enhanced collision kernels in turbulent clouds," *Atmos. Res.* **59-60**, 77 (2001).
- ⁷C. A. Vreugdenhil and J. R. Taylor, "Stratification effects in the turbulent boundary layer beneath a melting ice shelf: Insights from resolved large-eddy simulations," *J. Phys. Oceanogr.* **49**, 1905 (2019).
- ⁸C. Rorai, P. Mininni, and A. Pouquet, "Turbulence comes in bursts in stably stratified flows," *Phys. Rev. E* **89**, 043002 (2014).
- ⁹F. Feraco, R. Marino, A. Pumi, L. Primavera, P. Mininni, A. Pouquet, and D. Rosenberg, "Vertical drafts and mixing in stratified turbulence: Sharp transition with Froude number," *Europhys. Lett.* **123**, 44002 (2018).
- ¹⁰L. Browne, R. Antonia, and D. Shah, "Turbulent energy dissipation in a wake," *J. Fluid Mech.* **179**, 307 (1987).
- ¹¹A. Campagne, B. Gallet, F. Moisy, and P. P. Cortet, "Disentangling inertial waves from eddy turbulence in a forced rotating-turbulence experiment," *Phys. Rev. E* **91**, 043016 (2015).
- ¹²M. K. Sharma, M. K. Verma, and S. Chakraborty, "On the energy spectrum of rapidly rotating forced turbulence," *Phys. Fluids* **30**, 115102 (2018).
- ¹³Z. Yang, B.-Q. Deng, B.-C. Wang, and L. Shen, "The effects of streamwise system rotation on pressure fluctuations in a turbulent channel flow," *Phys. Fluids* **30**, 091701 (2018).
- ¹⁴S. T. Thoroddsen and C. W. van Atta, "The influence of stable stratification on small-scale anisotropy and dissipation in turbulence," *J. Geophys. Res.* **97**, 3647, <https://doi.org/10.1029/91jc02727> (1992).
- ¹⁵J. Werne and D. Fritts, "Anisotropy in a stratified shear layer," *Phys. Chem. Earth* **26**, 263 (2001).
- ¹⁶F. Godeferd and C. Staquet, "Statistical modelling and direct numerical simulations of decaying stably stratified turbulence. Part 2. Large-scale and small-scale anisotropy," *J. Fluid Mech.* **486**, 115 (2003).
- ¹⁷W. Smyth and J. Moum, "Anisotropy of turbulence in stably stratified mixing layers," *Phys. Fluids* **12**, 1343 (2000).
- ¹⁸G. A. Gerolymos and I. Vallet, "Destruction-of-dissipation and time-scales in wall turbulence," *Phys. Fluids* **31**, 055103 (2019).
- ¹⁹A. Garanaik and S. K. Venayagamoorthy, "On the inference of the state of turbulence and mixing efficiency in stably stratified flows," *J. Fluid Mech.* **867**, 323 (2019).
- ²⁰C. Lang and M. L. Waite, "Scale-dependent anisotropy in forced stratified turbulence," *Phys. Rev. Fluids* **4**, 044801 (2019).
- ²¹D. C. Fritts, L. Wang, J. Werne, T. Lund, and K. Wan, "Gravity wave instability dynamics at high Reynolds numbers. Part I: Wave field evolution at large amplitudes and high frequencies," *J. Atmos. Sci.* **66**, 1126 (2009).
- ²²P. Mininni, D. Rosenberg, R. Reddy, and A. Pouquet, "A hybrid MPI-OpenMP scheme for scalable parallel pseudospectral computations for fluid turbulence," *Parallel Comput.* **37**, 316 (2011).
- ²³D. Rosenberg, A. Pouquet, R. Marino, and P. Mininni, "Evidence for Bolgiano-Obukhov scaling in rotating stratified turbulence using high-resolution direct numerical simulations," *Phys. Fluids* **27**, 055105 (2015).
- ²⁴A. Pouquet, D. Rosenberg, R. Marino, and C. Herbert, "Scaling laws for mixing and dissipation in unforced rotating stratified turbulence," *J. Fluid Mech.* **844**, 519 (2018).
- ²⁵G. Ivey, K. Winters, and J. Koseff, "Density stratification, turbulence but how much mixing?," *Annu. Rev. Fluid Mech.* **40**, 169 (2008).
- ²⁶D. Rosenberg, R. Marino, C. Herbert, and A. Pouquet, "Variations of characteristic time-scales in rotating stratified turbulence using a large parametric numerical study," *Eur. Phys. J. E* **39**, 8 (2016).
- ²⁷R. Marino, D. Rosenberg, C. Herbert, and A. Pouquet, "Interplay of waves and eddies in rotating stratified turbulence and the link with kinetic-potential energy partition," *Europhys. Lett.* **112**, 49001 (2015).
- ²⁸P. Sagaut and C. Cambon, *Homogeneous Turbulence Dynamics* (Cambridge University Press, Cambridge, 2008).
- ²⁹R. Antonia, J. Kim, and L. Browne, "Some characteristics of small-scale turbulence in a turbulent duct flow," *J. Fluid Mech.* **233**, 369 (1991).
- ³⁰L. Djenidi, N. Lefeuvre, M. Kamruzzaman, and R. Antonia, "On the normalized dissipation C_ϵ in decaying turbulence," *J. Fluid Mech.* **817**, 61 (2017).
- ³¹A. Mashayek, H. Salehipour, D. Bouffard, C. Caulfield, R. Ferrari, M. Nikurashin, W. Peltier, and W. Smyth, "Efficiency of turbulent mixing in the abyssal ocean circulation," *Geophys. Res. Lett.* **44**, 6296, <https://doi.org/10.1002/2016gl072452> (2017).
- ³²L. Shih, J. Koseff, G. Ivey, and J. Ferziger, "Parameterization of turbulent fluxes and scales using homogeneous sheared stably stratified turbulence simulations," *J. Fluid Mech.* **525**, 193 (2005).
- ³³A. Maffioli, G. Brethouwer, and E. Lindborg, "Mixing efficiency in stratified turbulence," *J. Fluid Mech.* **794**, R3 (2016).
- ³⁴J. N. Moum, D. R. Caldwell, and C. A. Paulson, "Mixing in the equatorial surface layer and thermocline," *J. Geophys. Res.* **94**, 2005, <https://doi.org/10.1029/jc094i02p02005> (1989).
- ³⁵W. Smyth, J. Nash, and J. Moum, "Self-organized criticality in geophysical turbulence," *Sci. Rep.* **9**, 3747 (2019).
- ³⁶P. Mininni and A. Pouquet, "Inverse cascade behavior in freely decaying two-dimensional fluid turbulence," *Phys. Rev. E* **87**, 033002 (2013).
- ³⁷L. Mahrt and J. F. Howell, "The influence of coherent structures and microfronts on scaling laws using global and local transforms," *J. Fluid Mech.* **260**, 247 (1994).
- ³⁸A. Gargett, T. R. Osborn, and P. W. Nasmyth, "Local isotropy and the decay of turbulence in a stratified fluid," *J. Fluid Mech.* **144**, 231 (1984).
- ³⁹C. Rorai, D. Rosenberg, A. Pouquet, and P. Mininni, "Helicity dynamics in stratified turbulence in the absence of forcing," *Phys. Rev. E* **87**, 063007 (2013).
- ⁴⁰S. Chapman and N. Watkins, "Avalanching and self-organised criticality, a paradigm for geomagnetic activity?," *Space Sci. Rev.* **95**, 293 (2001).
- ⁴¹V. Uritsky, A. Pouquet, D. Rosenberg, P. Mininni, and E. Donovan, "Structures in magnetohydrodynamic turbulence: Detection and scaling," *Phys. Rev. E* **82**, 056326 (2010).
- ⁴²V. M. Uritsky, M. A. Roberts, C. R. DeVore, and J. T. Karpen, "Reconnection-driven magnetohydrodynamic turbulence in a simulated coronal-hole jet," *Astrophys. J.* **837**, 123 (2017).
- ⁴³L. Sorriso-Valvo, F. Catapano, A. Retinò, O. Le Contel, D. Perrone, O. W. Roberts, J. T. Coburn, V. Panebianco, F. Valentini, S. Perri *et al.*, "Turbulence-driven ion beams in the magnetospheric Kelvin-Helmholtz instability," *Phys. Rev. Lett.* **122**, 035102 (2019).
- ⁴⁴J. Wang, Q. Li, and W. E, "Study of the instability of the Poiseuille flow using a thermodynamic formalism," *Proc. Natl. Acad. Sci. U. S. A.* **112**, 9518 (2015).
- ⁴⁵G. Lemoult, L. Shi, K. Avila, S. V. Jalikop, M. Avila, and B. Ho, "Directed percolation phase transition to sustained turbulence in Couette flow," *Nat. Phys.* **12**, 254 (2016).
- ⁴⁶H.-Y. Shih, T.-L. Hsieh, and N. Goldenfeld, "Ecological collapse and the emergence of travelling waves at the onset of shear turbulence," *Nat. Phys.* **12**, 245 (2016).
- ⁴⁷Y. Pomeau, "Front motion, metastability and subcritical bifurcations in hydrodynamics," *Physica D* **23**, 3 (1986).
- ⁴⁸T. Dessup, L. S. Tuckerman, and J. E. Wesfreid, "Self-sustaining process in Taylor-Couette flow," *Phys. Rev. Fluids* **3**, 123902 (2018).
- ⁴⁹J. McWilliams, "Submesoscale currents in the ocean," *Proc. R. Soc. A* **472**, 20160117 (2016).
- ⁵⁰N. Sujovolsky, P. Mininni, and A. Pouquet, "Generation of turbulence through frontogenesis in sheared stratified flows," *Phys. Fluids* **30**, 086601 (2018).

- ⁵¹P. Vieillefosse, "Local interaction between vorticity and shear in a perfect incompressible fluid," *J. Phys.* **43**, 837 (1982).
- ⁵²C. Meneveau, "Lagrangian dynamics and models of the velocity gradient tensor in turbulent flows," *Annu. Rev. Fluid Mech.* **43**, 219 (2011).
- ⁵³N. Sujovolsky and P. Mininni, "Invariant manifolds in stratified turbulence," *Phys. Rev. Fluids* **4**, 052402 (2019).
- ⁵⁴G. E. Elsinga and I. Marusic, "The anisotropic structure of turbulence and its energy spectrum," *Phys. Fluids* **28**, 011701 (2016).
- ⁵⁵R. Grauer, J. Krug, and C. Mariani, "Scaling of high-order structure functions in magnetohydrodynamic turbulence," *Phys. Lett. A* **195**, 335 (1994).
- ⁵⁶H. Politano and A. Pouquet, "Model of intermittency in magnetohydrodynamic turbulence," *Phys. Rev. E* **52**, 636 (1995).
- ⁵⁷H. Politano, V. Carbone, and A. Pouquet, "Determination of anomalous exponents of structure functions in two-dimensional magnetohydrodynamic turbulence," *Europhys. Lett.* **43**, 516 (1998).
- ⁵⁸P. Mininni, A. Pouquet, and D. Montgomery, "Small-scale structures in three-dimensional magnetohydrodynamic turbulence," *Phys. Rev. Lett.* **97**, 244503 (2006).
- ⁵⁹R. Marino, L. Sorriso-Valvo, R. D'Amicis, V. Carbone, R. Bruno, and P. Veltri, "On the occurrence of the third-order scaling in high latitude solar wind," *Astrophys. J.* **750**, 41 (2012).
- ⁶⁰V. Petoukhov, A. Eliseev, R. Klein, and H. Oesterle, "On statistics of the free-troposphere synoptic component: An evaluation of skewnesses and mixed third-order moments contribution to the synoptic-scale dynamics and fluxes of heat and humidity," *Tellus A* **60**, 11 (2008).
- ⁶¹P. Sardeshmukh, G. P. Compo, and C. Penland, "Need for caution in interpreting extreme weather statistics," *J. Clim.* **28**, 9166 (2015).
- ⁶²C. Cambon and L. Jacquin, "Spectral approach to non-isotropic turbulence subjected to rotation," *J. Fluid Mech.* **202**, 295 (1989).
- ⁶³R. A. Antonia, L. Djenidi, and P. R. Spalart, "Anisotropy of the dissipation tensor in a turbulent boundary layer," *Phys. Fluids* **6**, 2475 (1994).
- ⁶⁴G. D. Portwood, S. M. de Bruyn Kops, J. Taylor, H. Salehipour, and C. P. Caulfield, "Robust identification of dynamically distinct regions in stratified turbulence," *J. Fluid Mech.* **807**, R2 (2016).
- ⁶⁵W. Bos, L. Liechtenstein, and K. Schneider, "Small-scale intermittency in anisotropic turbulence," *Phys. Rev.* **76**, 046310 (2007).
- ⁶⁶R. Hide, "A note on helicity," *Geophys. Fluid Dyn.* **7**, 157 (1976).
- ⁶⁷R. Marino, P. Mininni, D. Rosenberg, and A. Pouquet, "Emergence of helicity in rotating stratified turbulence," *Phys. Rev. E* **87**, 033016 (2013).
- ⁶⁸B. Koprov, V. Koprov, V. Ponomarev, and O. Chkhetiani, "Experimental studies of turbulent helicity and its spectrum in the atmospheric boundary layer," *Dokl. Phys.* **50**, 419 (2005).
- ⁶⁹P. Mininni and A. Pouquet, "Helicity cascades in rotating turbulence," *Phys. Rev. E* **79**, 026304 (2009).
- ⁷⁰L. Mahrt, "Stably stratified atmospheric boundary layers," *Annu. Rev. Fluid Mech.* **46**, 23 (2014).
- ⁷¹V. Giddey, D. W. Meyer, and P. Jenny, "Modeling three-dimensional scalar mixing with forced one-dimensional turbulence," *Phys. Fluids* **30**, 125103 (2018).
- ⁷²R. Maulik, O. San, A. Rasheed, and P. Vedula, "Data-driven deconvolution for large eddy simulations of Kraichnan turbulence," *Phys. Fluids* **30**, 125109 (2018).
- ⁷³S. Heinz, "The large eddy simulation capability of Reynolds-averaged Navier-Stokes equations: Analytical results," *Phys. Fluids* **31**, 021702 (2019).
- ⁷⁴H. W. Wijesekera, J. S. Allen, and P. A. Newberger, "Modeling study of turbulent mixing over the continental shelf: Comparison of turbulent closure schemes," *J. Geophys. Res.* **108**, 25, <https://doi.org/10.1029/2002jc001408> (2003).
- ⁷⁵S. E. Belcher, A. L. M. Grant, K. E. Hanley, B. Fox-Kemper, L. V. Roedel, P. P. Sullivan, W. G. Large, A. Brown, A. Hines, D. Calvert *et al.*, "A global perspective on Langmuir turbulence in the ocean surface boundary layer," *Geophys. Res. Lett.* **39**, L18605, <https://doi.org/10.1029/2012gl052932> (2012).